Structural details of Al/Al_2O_3 junctions and their role in the formation of electron tunnel barriers

M. Koberidze,* M. J. Puska, and R. M. Nieminen
COMP Center of Excellence, Department of Applied Physics, Aalto University School of Science, P.O. Box 11100, FI-00076 Aalto, Finland

(Received 5 December 2017; revised manuscript received 15 February 2018; published 4 May 2018)

We present a computational study of the adhesive and structural properties of the Al/Al_2O_3 interfaces as building blocks of the metal-insulator-metal (MIM) tunnel devices, where electron transport is accomplished via tunneling mechanism through the sandwiched insulating barrier. The main goal of this paper is to understand, on the atomic scale, the role of the geometrical details in the formation of the tunnel barrier profiles. Initially, we concentrate on the adhesive properties of the interfaces. To provide reliable results, we carefully assess the accuracy of the traditional methods used to examine Al/Al_2O_3 systems. These are the most widely employed exchange-correlation functionals—local-density approximation and two different generalized gradient approximations; the universal binding-energy relation for predicting equilibrium interfacial distances and adhesion energies; and the ideal work of separation as a measure of junction stability. In addition, we show that the established interpretation of the computed ideal work of separation might be misleading in predicting the optimal interface structures. Finally, we perform a detailed analysis of the atomic and interplanar relaxations in each junction, and identify their contributions to the tunnel barrier parameters. Our results imply that the structural irregularities on the surface of the Al film have a significant contribution to lowering the tunnel barrier height, while atomic relaxations at the interface and interplanar relaxations in Al_2O_3 may considerably change the width of the barrier and, thus, distort its uniformity. Both the effects may critically influence the performance of the MIM tunnel devices.

DOI: 10.1103/PhysRevB.97.195406

I. INTRODUCTION

Metal-insulator-metal (MIM) tunnel junctions are principal components of numerous modern nanoelectronic devices. The operation of such devices is based on electron tunneling across MIM systems from one metal to the other. The most common choice for the metal is Al, and for the insulator the most common choice is its native oxide, Al_2O_3. Thus, the Al/Al_2O_3 junction is the most widely used base structure in MIM tunneling devices, particularly for applications such as quantum computing, ultrasensitive magnetometry, radiation detection, and quantum metrology [1,2].

It has been shown that the electron transport properties of Al/Al_2O_3-based tunnel devices are strongly affected by the atomic structure near the interface between Al and Al_2O_3 [3–6], as well as by the variation in the thickness of the oxide layer throughout the junction [7–9]. Structural defects at the interface [3,5], roughness of the metal substrate [4,10,11] and nonuniformity of the oxide thickness [3,7,8] are anticipated to be the critical factors, which may deteriorate the functionality of the oxide as a barrier. However, characterization of this impact is in its early stage and hence still uncertain. Understanding the subtle relationship between the geometry of the Al/Al_2O_3 junctions and the tunneling properties on the atomistic level would help to achieve a better control and an improved performance of MIM devices. Therefore, careful atomistic characterization of the interface is essential.

Although the structure of Al/Al_2O_3 systems has actively been explored over the decades both theoretically [12–19] and experimentally [4,5,9,20–24], an in-depth understanding of the interface properties is still an ongoing issue. Experimental observations have provided valuable information, for example, about the most probable crystallographic orientation relationship between Al and Al_2O_3 at the interface [21,23], Al substrate roughness [4,20], the chemical state of the ions [25], oxide thickness distribution [9], bond lengths and coordinations of the atoms [5] at the interface, Al/O ratios for different oxide thicknesses [24], and different oxidation times and temperatures [25]. However, experimental determination of the detailed atomic structures of the buried ultrathin interfaces is challenging. Additionally, the structure of the formed interface depends on the oxidation method and on the oxidation parameters [9,25,26]. This further complicates obtaining consistent experimental data about the atomic details of the interface geometry and their effects on the tunneling properties. For these reasons, availability of accurate and reliable theoretical predictions is particularly important.

Despite the significance of the Al/Al_2O_3 junctions, and popularity of the density functional theory (DFT) method for quantum mechanical description of the many-body systems, the first DFT studies on Al/Al_2O_3 interfaces appeared relatively late. Pioneering DFT works addressed the atomic structures of differently constructed Al/Al_2O_3 interfaces, bonding at the interface, adhesion energies, and the most stable terminations of the oxide at the interface [12–14,27,28]. More recent DFT studies are focused on improving junction models and on screening possibilities for improved adhesion, which is the measure of the structural stability of the system [16,17,19].

Nevertheless, how the structure and geometry of the Al/Al_2O_3 interfaces relate to the tunneling properties of Al/Al_2O_3-based devices is barely known. In our previous

*manana.koberidze@aalto.fi

study [6], we demonstrated the effect of the different interface structures on the tunnel barrier heights and widths for the $Al/Al_2O_3/Al$ tunnel junctions. The work was based on the analysis of experimental current-voltage (IV) data using analytic models for tunneling current, where the employed barrier parameters were those predicted by DFT. In the current paper, first, we explain the procedure for obtaining the model Al/Al_2O_3 junctions used in our preceding work. Next, we present detailed structural analyses of the model systems to understand the role of atomic-scale geometrical variations in the formation of tunnel barriers. Particularly, we identify the factors affecting the height of the tunnel barrier, and those contributing to the thickness variation of the oxide. To the best of our knowledge, none of the previous theoretical studies has addressed the structural details of the Al/Al_2O_3 junctions in connection with the tunnel barrier profiles, nor have factors contributing to the nonuniformity of the oxide barrier been investigated theoretically.

Since tunneling properties of the MIM systems are sensitive to the interface geometry, when modeling tunnel junctions, obtaining reliable optimal structures and performing careful analysis are critical. Therefore, we pay particular attention to validating the applied methods. For the DFT calculations, we choose the exchange-correlation functional after evaluating the accuracy of the most commonly used functionals for the Al/Al_2O_3 systems. We also assess the accuracy of the universal binding-energy relation (UBER), which is commonly adopted for determining equilibrium interfacial distances and equilibrium adhesion energies. In addition, we challenge the reliability of conventional interpretation of the computed ideal work of adhesion as a measure of the interface stability.

Having examined the performance of the different methods and identified the most accurate ones for our systems, we construct the optimal model interfaces. In the end, we look into the correlation between the geometrical structure and the tunnel barrier profile. For this purpose, we analyze the atomic as well as interplanar relaxations. Atomic positions at the interface play an important role in defining the magnitude of tunnel barrier heights. Interplanar relaxations beyond the immediate interface affect the width of the tunnel barrier and contribute to the thickness variation of the oxide. Even a tiny change in the width of the barrier significantly impacts on the functionality of the MIM tunnel devices, since the tunneling probability depends exponentially on the barrier width.

The present paper is organized as follows: In Sec. II, we describe our calculation setup and discuss the performance of different exchange-correlation functionals in predicting the bulk and surface properties of Al and Al_2O_3. In Secs. III A–III C, we describe the procedure for setting up the model interfaces and a step-by-step validation of the applied methods. Sections III D and III E include the analysis of the atomic and interplanar relaxations, respectively, and their connections to the tunnel barrier profiles. Section IV provides a short summary of our findings.

II. CALCULATION METHOD

In all the calculations presented in this paper, we use the DFT within the projector-augmented wave code GPAW [29,30]. Until recently, the most frequently used exchange-correlation functionals for Al/Al_2O_3 interfaces have been the local-density approximation (LDA) [14,27] and the generalized gradient approximations (GGAs) [3,14–17]. To identify the most suitable one for our calculations, we compared the accuracy of the three density functionals, LDA by Perdew and Wang [31], and the two GGAs by Perdew, Burke and Ernzerhof (PBE) [32] and by Perdew *et al.* (PW91) [33], in predicting equilibrium lattice constants (a_0, c_0), cohesive energies (E_c), and bulk moduli (B) of the bulk materials, as well as interplanar space relaxations (Δd) and surface energies (σ) of the slabs.

In our setup, as a starting point, both the Al and Al_2O_3 unit-cell dimensions are set corresponding to the experimental lattice constants. That is, for the cubic Al, $a_0 = 4.05$ Å [34], and, for the hexagonal Al_2O_3, $a_0 = 4.759$ Å, $c_0 = 12.991$ Å [35]. For our bulk calculations, Al is represented with a hexagonal unit cell containing 12 atoms. We use the $(14\times14\times14)$ Monkhorst-Pack grid to sample the Brillouin zone and the 0.18-Å real-space grid spacing.

For the bulk α-Al_2O_3, we use a hexagonal unit cell as well, containing 30 atoms, among them 12 Al and 18 O. We employ the $(4\times4\times4)$ Monkhorst-Pack grid, and the 0.13-Å real-space grid spacing. In all the calculations, the electron occupation function is represented with the Fermi-Dirac distribution at the 0.1-eV electronic temperature. With these parameters, the total energy per atom for both the materials is converged to within 1 meV. We find the equilibrium lattice constants (a_0), bulk moduli (B), and cohesive energies (E_c) from the equation of state. For this purpose, we strain the initial volumes isotropically by factors between 0.95 and 1.05 and calculate energy-versus-volume curves using ten equally spaced points. We use the Murnaghan function [36] to fit to the calculated points.

For constructing the Al and Al_2O_3 surfaces, we use the same experimental lattice constants as for setting up the bulk materials. We use the two-dimensional periodic slab model, which is periodic in the interface (xy) plane and nonperiodic along the z axis. We add 5-Å vacuum on both surfaces of the slabs. We carry out calculations with the $(4\times4\times1)$ Monkhorst-Pack grid for the Al metal and the $(14\times14\times1)$ grid for the Al_2O_3 oxide. The real-space grid spacings are the same as in the bulk calculations.

Keeping in mind that our model slabs are constituents of the junctions in our interface calculations, we study the Al(111) and Al_2O_3 (0001) surface orientations and fix the lateral lattice constants at the experimental values during the relaxation of the surfaces (the choice is explained in the following section). The Al(111) and Al_2O_3 (0001) slabs are composed of 5 and 18 layers, respectively. Each layer of the Al slab contains three atoms, resulting in 15 atoms in total. The oxide slab is composed of six units of Al_2O_3, i.e., 30 atoms in total. During the structural optimization of the slabs, vertical relaxation is unconstrained and facilitated by the presence of the vacuum layer. The structures are relaxed until forces on each atom are less than 0.01 eV/Å.

The comparison of the three exchange-correlation functionals in predicting the bulk and surface properties of Al and Al_2O_3 shows that the GGA functionals provide a significantly better description of the bulk properties and surface relaxations of Al as well as the cohesive energies of both the materials compared to LDA. At the same time, they produce acceptable errors for the oxide properties, which are best described

with LDA. The two GGAs do not exhibit major differences in their performances; however, on average, PBE predicts the properties of Al slightly more accurately than PW91. Therefore, we choose to continue calculations with the PBE functional. More details on the accuracy of each functional and our calculated parameters are reported in the Appendix.

III. Al/Al_2O_3 INTERFACES

A. Setting up model interfaces

When setting up different interfaces, we follow the procedure presented in Ref. [14]. We start constructing the interfaces with five-layer Al(111) and 18-layer Al_2O_3 (0001) slabs. It has been shown previously that five layers of Al(111) and 15 layers of Al_2O_3 (0001) are enough to converge the surface energies and the surface relaxations [14]. However, we have represented the oxide with its complete hexagonal unit cell with 18 layers, which would be sufficient for recovering the ordered structure. This is relevant to our calculations, since we are interested in the geometry of the whole oxide film, at the interface and beyond it. With the chosen surface orientations, the crystallographic structures of Al and Al_2O_3 are best matched. The same preferred orientations have also been verified in experiments [21]. Neither of the slabs is relaxed beforehand and the initial lattice constants correspond to the experimental values. Due to the difference in the lattice constants of the two materials, one of them should be strained. Since Al has a smaller bulk modulus and is softer than Al_2O_3, we compress Al in the xy plane to match the lattice of the oxide, as often done in other works as well [13,14,17]. This means that the lateral lattice constant a of our model junction corresponds to the experimental lattice constant of Al_2O_3, 4.759 Å. Another option could be the use of the equilibrium lateral lattice constants predicted by the chosen exchange-correlation functional for the bulk systems. However, based on our calculations, the lattice mismatch $[a(\mathrm{Al})\text{-}a(\mathrm{Al_2O_3})]/a(\mathrm{Al})$, where a denotes the length of the in-plane lattice translation vector, is 2.4% as suggested by PBE, while the experimentally evaluated mismatch amounts to 4.3% [21]. We assume that maintaining the lattice mismatch close to the experimental value will yield a more realistic description of the junction.

Since it is impossible to study the whole configurational space for adhesion between the two surfaces, we consider three different stacking sequences between the facing Al and Al_2O_3 surface layers, and two possible terminations of the oxide (a single Al or O layer), i.e., six configurations in total. For the stacking sequence we examine the fcc, hcp, and octahedral (ot) sites. The fcc stacking labels the interface, where the Al surface atoms of the metal and those of the oxide sit on top of each other (see unrelaxed structures in Fig. 1), the hcp stacking means that the surface Al atoms are placed along the second O layer of the oxide, and in the ot stacking the Al atoms of the metal sit on top of the first O layer of the oxide. In Fig. 1, the z axis is chosen perpendicularly to the interface. The whole system consists of 45 atoms for all geometries.

All the calculations on interfaces are performed with the $(4\times4\times1)$ k-point grid and a real-space grid spacing of 0.13 Å. A 5-Å-vacuum layer is added on each side of the slab. We employ an asymmetric model, where the system is nonperiodic in the direction perpendicular to the interface (along the z axis). Thus, periodic boundary conditions are applied only on the xy plane. To eliminate an artificial electric field due to the asymmetry of the slab, we apply the dipole correction to the electrostatic potential along the z axis as implemented in GPAW. We have chosen such a construction of the interface over the periodic supercell model because the presence of a vacuum layer in the asymmetric model allows full vertical relaxation of the structure, which is expected due to the lateral strain on Al and possible interfacial stresses. Conversely, in the supercell approach without a vacuum layer, translational freedom is restricted in the z direction by the dimensions of the simulation box. Besides, the asymmetric structure more closely resembles the Al/Al_2O_3 junction in experiments where the interface is indeed prone to relaxation before depositing the second electrode, while in the supercell model Al/Al_2O_3 stacks are assumed to form an infinite array. Thus, our choice of the setup enables us to characterize the interface without imposing restrictions to the interplanar relaxations and without the influence of the second electrode. Advantages and disadvantages of the two methods are discussed, for example, in Ref. [37, Chap. 5.2.2].

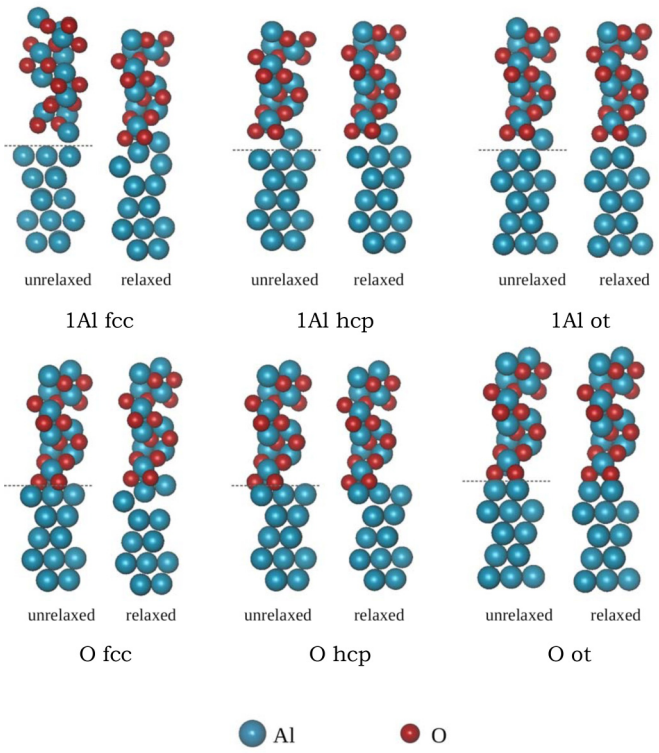

FIG. 1. The six modeled interfaces. Upper panel: The junctions with the initially Al-terminated oxides and three different stacking sequences at the interfaces. Lower panel: The junctions with the initially O-terminated oxides and with the same stacking sequences as in the Al-terminated structures. The dashed lines on the unrelaxed systems show the boundary between the metal and the oxide slabs separated by the distance d_0. The procedure for finding d_0 is explained in the text.

B. Adhesion and separation at the interface

The distance at which the Al and Al_2O_3 slabs should be placed, in order to form the minimum-energy configuration,

TABLE I. Comparison of UBER and fifth-order spline fits for finding the optimal distance d_0 between the unrelaxed slabs. Errors are evaluated with respect to the DFT values. $W_{\mathrm{DFT}}(d_{0_{\mathrm{UBER}}})$ and $W_{\mathrm{DFT}}(d_{0_{\mathrm{spline}}})$ are adhesion energies calculated with DFT at d_0 predicted by UBER and the spline fits, respectively.

	$d_{0_{\mathrm{UBER}}}$ (Å)	$W_{0_{\mathrm{UBER}}}$ (J/m^2)	$W_{\mathrm{DFT}}(d_{0_{\mathrm{UBER}}})$ (J/m^2)	$\mathrm{Error}_{\mathrm{UBER}}$ (%)	$d_{0_{\mathrm{spline}}}$ (Å)	$W_{0_{\mathrm{spline}}}$ (J/m^2)	$W_{\mathrm{DFT}}(d_{0_{\mathrm{spline}}})$ (J/m^2)	$\mathrm{Error}_{\mathrm{spline}}$ (%)
1Al fcc	2.66	1.13	1.04	8.65	2.59	1.05	1.05	0.00
1Al hcp	2.47	1.13	1.12	0.89	2.40	1.14	1.13	0.88
1Al ot	2.30	1.26	1.29	−2.32	2.24	1.30	1.30	0.00
O fcc	1.41	6.95	6.61	5.14	1.47	6.84	6.78	0.88
O hcp	1.34	7.52	6.91	8.83	1.40	7.31	7.09	3.10
O ot	1.74	7.46	7.41	0.67	1.73	7.41	7.41	0.00

can be found by calculating the *ideal work of adhesion* per unit area W_{Adh} as a function of the interfacial distance d. W_{Adh} is defined as

$$W_{\mathrm{Adh}} = (E_{\mathrm{Al}} + E_{\mathrm{Al_2O_3}} - E_{\mathrm{int}})/A, \tag{1}$$

where E_{Al} and $E_{\mathrm{Al_2O_3}}$ are the total energies of the isolated Al and Al_2O_3 slabs, respectively, and E_{int} is the total energy of the whole system. A is the area of the interface. Thus, W_{Adh} is equivalent to the energy needed to separate the two slabs infinitely from each other and has a positive sign for the bound system in equilibrium. Often in literature, the ideal work of adhesion is also referred as "the ideal work of separation" [38,39]. $-W_{\mathrm{Adh}}$ can be interpreted as the *adhesive binding energy* of the two films in the junction.

A standard method for finding the optimal distance between the two slabs in the junction system is to first calculate $-W_{\mathrm{Adh}}$ at several distances with DFT. Next, a known analytic function is fitted to the obtained points, and the equilibrium separation d_0 is identified where the minimum of the fit function occurs. The widely used analytic form for the adhesive binding energy is UBER [40]:

$$W_{\mathrm{UBER}}(d) = -W_0(1 + d_s)\exp(-d_s), \tag{2}$$

where $d_s = (d - d_0)/l$ is a scaling length, l is a scaling parameter to be fitted, and W_0 is the fitted adhesion energy at the equilibrium separation d_0. UBER has been widely applied to various materials and interfaces, including Al/Al_2O_3 junctions [14]. However, to our knowledge, the accuracy of UBER, specifically for Al/Al_2O_3 interfaces, has not been examined. Since the purpose of this paper is to characterize Al/Al_2O_3 interfaces as components of tunnel devices, we consider the accurate determination of the metal-oxide separation particularly important.

UBER was developed to describe metallic and covalent bonds [40–42] and might not be reliable for ionic solids. This dictates that we might expect the most reasonable description for the 1Al fcc structure in the case in which the (unrelaxed) interface bonding is primarily formed via the Al-Al bonds. In contrast, the method might be particularly inaccurate in the case of the oxygen-terminated Al_2O_3 where ionic bonding dominates. Therefore, the applicability of UBER to our Al/Al_2O_3 systems has to be checked. For this purpose, we first predict d_0 and W_{Adh} values using UBER, as well as using the fifth-order spline fit to the DFT points (Fig. 2). Next, we place the Al and Al_2O_3 layers at the distance $d_{0_{\mathrm{UBER}}}$ ($d_{0_{\mathrm{spline}}}$) and calculate the adhesion energies with DFT, one at the interfacial distance predicted by UBER [$W_{\mathrm{DFT}}(d_{0_{\mathrm{UBER}}})$] and the other at the interfacial distance predicted by the fifth-order spline [$W_{\mathrm{DFT}}(d_{0_{\mathrm{spline}}})$]. The accuracies of the two fits are analyzed in Table I. When compared to the DFT results, the spline fit produces smaller errors than the UBER fit for all geometries.

The spline interpolation results in 0–2.6% higher adhesion energies compared to those obtained using UBER. This means that the former predicts an interfacial distance at which adhesion is stronger, that is, it predicts the equilibrium structure more accurately. On average, relative to the spline interpolation, UBER overestimates the interfacial distance for the Al-layer terminated structures by 2.8%, and underestimates it for the O-layer terminated structures by 2.6%. Nevertheless, UBER is usually a good enough approximation. However, as the accuracy of the interface geometry is crucial, we decide to use d_0 predicted by the spline fitting.

Finally, to set up the junction, we place the unrelaxed Al and Al_2O_3 slabs at the distances found from fitting and relax the entire structure. Relaxation results in the decrease of adhesion energy W_0 in all the Al-terminated interfaces, while in all the O-terminated cases the effect is opposite (Table II). The same trend has been observed for other metal/Al_2O_3 junctions as well [13]. Even though structural relaxation leads to minimizing the total energy of a system, the same is not necessarily fulfilled for the adhesion energy. Whether W_0 increases or decreases following the relaxation is defined by the *change* in each term of Eq. (1). For example, increase in the case of the O-terminated structures means that the net decrease in

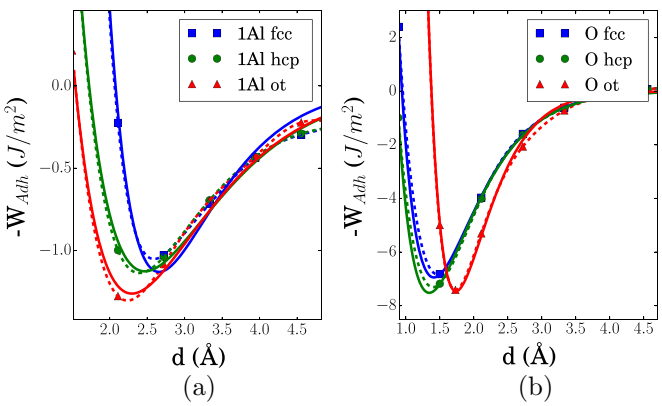

FIG. 2. Adhesive binding energy as a function of the interfacial distance d for the Al-terminated (a) and O-terminated (b) structures. The discrete data points are $-W_{\mathrm{adh}}$ obtained from the DFT calculations. The solid lines are UBER fits to the DFT points. The dashed lines represent the fifth-order spline fit.

TABLE II. Effect of relaxation on W_0 and d_0. Arrows up indicate increase after relaxation, arrows down indicate decrease, and ∼ denotes an almost unchanged value. $d_{0(\mathrm{LDA})}$ and $W_{0(\mathrm{GGA})}$ are the equilibrium interfacial distance and adhesion energy, respectively, taken from Ref. [14], where $d_{0(\mathrm{LDA})}$ was calculated with LDA, and $W_{0(\mathrm{GGA})}$ with PW91 after preceding relaxations with LDA.

	Before relaxation		After relaxation		Effect of relaxation		Ref. [14]	
	d_0 (Å)	W_0 (J/m^2)	d_0 (Å)	W_0 (J/m^2)	d_0 (Å)	W_0 (J/m^2)	$d_{0(\mathrm{LDA})}$ (Å)	$W_{0(\mathrm{GGA})}$ (J/m^2)
1Al fcc	2.59	1.05	0.97	0.84	↓	↓	0.70	1.06
1Al hcp	2.40	1.13	2.55	0.48	↑	↓	2.57	0.41
1Al ot	2.24	1.30	2.29	0.70	↑	↓	1.62	0.84
O fcc	1.47	6.78	0.87	8.48	↓	↑	0.86	9.73
O hcp	1.40	7.09	1.23	7.97	↓	↑	1.06	9.11
O ot	1.73	7.41	1.72	8.05	∼	↑	2.00	8.75

the total energies of the slabs is smaller than the decrease in the total energy of the junction, $\Delta(E_{\mathrm{Al}}) + \Delta(E_{\mathrm{Al_2O_3}}) < \Delta(E_{\mathrm{int}})$.

For the Al-terminated cases, the adhesion energy decreases in the order fcc, hcp, ot, while the interfacial distance d_0 increases in the same order. The trend agrees with the results reported in Ref. [14]. For the O-terminated structures d_0 has the same trend as that for the Al-terminated cases, while W_0 decreases in the order fcc, ot, hcp. This sequence differs from that obtained in Ref. [14], and our predicted values for the adhesion energies are, in general, smaller. The fcc stackings exhibit the highest adhesion energies and smallest interfacial distances in agreement with Ref. [14].

C. W_{Adh} as a measure of stability

In the existing studies, detailed analyses of the interfaces with hcp and ot stacking are most often overlooked. Usually, the fcc-stacked interfaces are claimed to be the most stable structures and are examined as representatives of the junctions [12,14,16]. One reason is the fact that these are the structures which exhibit the most dramatic atomic relaxations at the interfaces. Another reason is that, according to the DFT calculations, the fcc stacking yields the highest ideal work of separation, interpreted as an indicator of the most stable configurations. Interestingly, in our previous study [6], by combining DFT, analytic models for tunneling current, and experimental data, we estimated that the most dominant geometry in the Al/Al_2O_3 junction should be 1Al ot followed by 1Al hcp.

Although the strongest interfacial adhesion should indeed mean the highest stability, the interpretation of W_{Adh} for the relaxed interfaces should be considered more carefully: the definition of W_{Adh} based on Eq. (2) in the case of the unrelaxed structures is straightforward and unambiguous since the constituent slabs in the unrelaxed interfaces are structurally identical to the separate isolated slabs. In contrast, comparing the energy of the relaxed joint system to that of the isolated relaxed slabs is vague, since Al or Al_2O_3, relaxed as parts of the junction, and respective independent slabs relaxed in vacuum, are not structurally identical. In addition to probable adjustments of the interplanar distances, the interface relaxation may cause changes in the local stoichiometry of Al_2O_3 and/or in the coordination of the Al atoms near the interface. Thus, in the case of the relaxed interfaces, the definition of W_{Adh} implies that if the junction was to be separated into the Al and Al_2O_3 parts they would instantly adopt the geometry of the isolated slabs relaxed in vacuum. Such a definition neglects structural changes at the interface due to the relaxation. Moreover, whether in this way estimated W_{Adh} is the measure of the adhesion between the immediate Al and Al_2O_3 surfaces becomes ambiguous, since the termination or the beginning of either material in the interface region might no longer be well defined in the relaxed junctions. Therefore, such a description leads to the inaccurate understanding of the interfacial adhesion strength and, consequently, of the stability of the junctions. To address the issue, we estimated the stability of the junctions by subtracting atomic energies from the total energy of the systems, analogous to calculating cohesive energies of the bulk materials: $\Delta E = N_{\mathrm{O}}E_{\mathrm{O}} + N_{\mathrm{Al}}E_{\mathrm{Al}} - E_{\mathrm{int}}$, where ΔE is the binding energy of the system, and N_{O} and N_{Al} are the numbers of O and Al atoms in the junctions, respectively. E_{O} and E_{Al} are the spin-polarized total energies of O and Al atoms, respectively, and E_{int} is the total energy of the system. While ΔE will not give information about the adhesion strengths between any two neighboring layers, it provides an average estimate of the relative stabilities of the different junctions. Since the equilibrium structure adopted by a bound system is the one with the strongest bonding, i.e., with the highest cohesive energy, by estimating ΔE, we can identify energetically the most favorable interface configurations. Obtained cohesive energies are presented in Table III.

ΔE for all the O-terminated structures are smaller than those for the Al-terminated interfaces. This implies that, in general, junctions with 1Al-terminated interfaces are more strongly bound compared to those with O-terminated interfaces. More importantly, 1Al ot is, energetically, almost as favorable as 1Al fcc, supporting our prediction in the previous work based on the analysis of the experimental current-voltage characteristics. Our results emphasize that relying on the W_{Adh} predictions for identifying the most stable joint systems can be misleading, and results in ignoring other possible interface configurations, which might be present in real junctions,

TABLE III. Binding energies ΔE of different Al/Al_2O_3 structures. Each system contains 45 atoms.

Geometry	1Al fcc	1Al hcp	1Al ot	O fcc	O hcp	O ot
ΔE (eV)	231.38	230.94	231.21	230.00	229.37	229.47

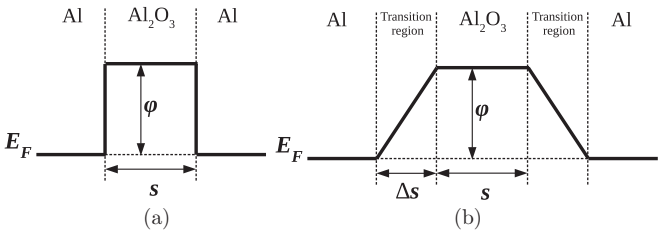

FIG. 3. Profiles of the tunnel barriers according to the (a) rectangular and (b) trapezoidal models. ϕ is the tunnel barrier height, s is the width of the barrier, and Δs is the width of the metal-oxide transition region. The barrier profile is defined with respect to the Fermi level E_F of the metal.

and have a significant contribution to the potential barrier parameters.

D. Atomic relaxations at the Al/α-Al_2O_3 interfaces

As mentioned in the introduction, the atomic structure of the interface has a critical impact on the behavior of the MIM devices, especially on the functionality of the oxide barrier. In the current section, we will examine the geometries of the different interfaces formed between Al and Al_2O_3, and investigate their relation to the properties of the tunnel barriers. The tunnel barriers are traditionally modeled using rectangular [43–46] and sometimes trapezoidal [47] barrier models. The two models are shown in Fig. 3. The rectangular barrier model assumes an abrupt interface between the metal and the oxide, while the trapezoidal barrier model allows for a finite-width metal-oxide transition region. The transition region can be formed as a result of interfacial relaxations and its atomic structure might not correspond to the ordered crystalline structure of either the metal or the oxide. Its width characterizes the abruptness of the interface and contributes to the total width of the barrier.

By combining the trapezoidal model, the DFT method, and experimental data for the conductance, we previously evaluated barrier heights (ϕ), barrier widths (s), and the widths of the metal-oxide transition regions (Δs) for the six $Al/Al_2O_3/Al$ junctions with the same Al/Al_2O_3 interface geometries, which are studied in the current paper (Table IV). We found striking differences in the barrier heights and widths, and also a large scatter in the widths of the metal-oxide transition regions, which emphasizes the strong sensitivity of ϕ, s, and Δs to the atomic structure of the interface region. Below, we will look into the reasons behind these distinctions. To identify the factors affecting the three parameters (width, height, and abruptness), and to associate them with the geometrical patterns of the interface, first, we will investigate the atomic structures in the interface regions following the relaxations. In the next section, we will study the structural characteristics of the junctions beyond the immediate interfaces, and their possible impacts on the tunnel barrier profiles.

TABLE IV. Barrier parameters for the Al/Al_2O_3 interfaces from Ref. [6]. ϕ is the barrier height, Δs is the width of the transition region, and s is the width of the barrier.

	ϕ(eV)	Δs(Å)	s(Å)
1Al fcc	1.2	5.8	8.9
1Al hcp	3.2	2.8	6.8
1Al ot	2.7	2.6	7.6
O fcc	1.3	3.3	10.3
O hcp	1.3	3.2	10.5
O ot	1.8	2.1	9.7

Atomic rearrangements at the interfaces due to the relaxations vary with the oxide termination and the stacking sequence of the joined surfaces (Fig. 4). Displacements are significant along the z direction. The center-of-mass translation occurs both in the metal and in the oxide parts. This indicates at the adjusted interplanar distances near (and possibly beyond) the interfaces associated with the interfacial stress release. Structural changes in the interface regions arise mainly due to the relaxations of the interfacial Al atoms belonging to the metal films. Such rearrangements alter the width of the transition region between the metal and the oxide films. Figures 1 and 4 show that it may either be relatively abrupt or span several atomic layers depending on the stacking and the oxide termination, and it is primarily composed of Al atoms displaced from the surface of the metal film. The effect is particularly notable for the 1Al fcc and O fcc junctions, where Al atom(s) from the surface layers of the respective metal films are translated towards the first oxide layer at the interface, complementing the stoichiometry of the Al_2O_3 unit [Figs. 4(a) and 4(d)]. The metal surface is similarly distorted in the O hcp system, though to a smaller extent [Fig. 4(e)]. The stoichiometric extension of the oxide does not occur due to the unfavorable positions of the interface Al and O layers with respect to each other.

In the remaining three junctions—1Al hcp, 1Al ot, and O ot—rearrangements of the atoms near the interface, belonging to the metal film, are relatively small. Thus, while relaxing the interface, the oxide film tries to extend its crystalline structure by adopting Al atoms from the metal surface within the available space for relaxation, as also observed in earlier studies [14,17]. This creates roughness and deficiency of Al atoms on the surface of the metal film, and changes the thickness and the terminating layer of the oxide. Short-range roughness on the surface of the metal substrate in Al/Al_2O_3 junctions, with the height of one or two Al(111) interplanar spacings, has also been observed experimentally [20]. Moreover, experimental studies have shown that the surface roughness of the metal film strongly influences the conductive properties of the MIM junctions [4,10,48].

Referring to Table IV, the junctions with the most distorted metal surfaces—1Al fcc, O fcc, and O hcp—have the widest transition regions (Δs) in the decreasing order. This indicates that the roughness of the metal surface is a primary cause for the finite-width transition region, and that a rougher surface implies a wider Δs. The observed correlation is limited to a qualitative conclusion, since a quantitative description of the roughness would require modeling much larger interfaces, which is challenging within the standard DFT method. Table IV also shows that the same three structures are characterized with the smallest barrier heights among all the considered junctions. Thus, our results suggest that deviation from coplanarity of the metal surface layers has a critical role in the formation of the

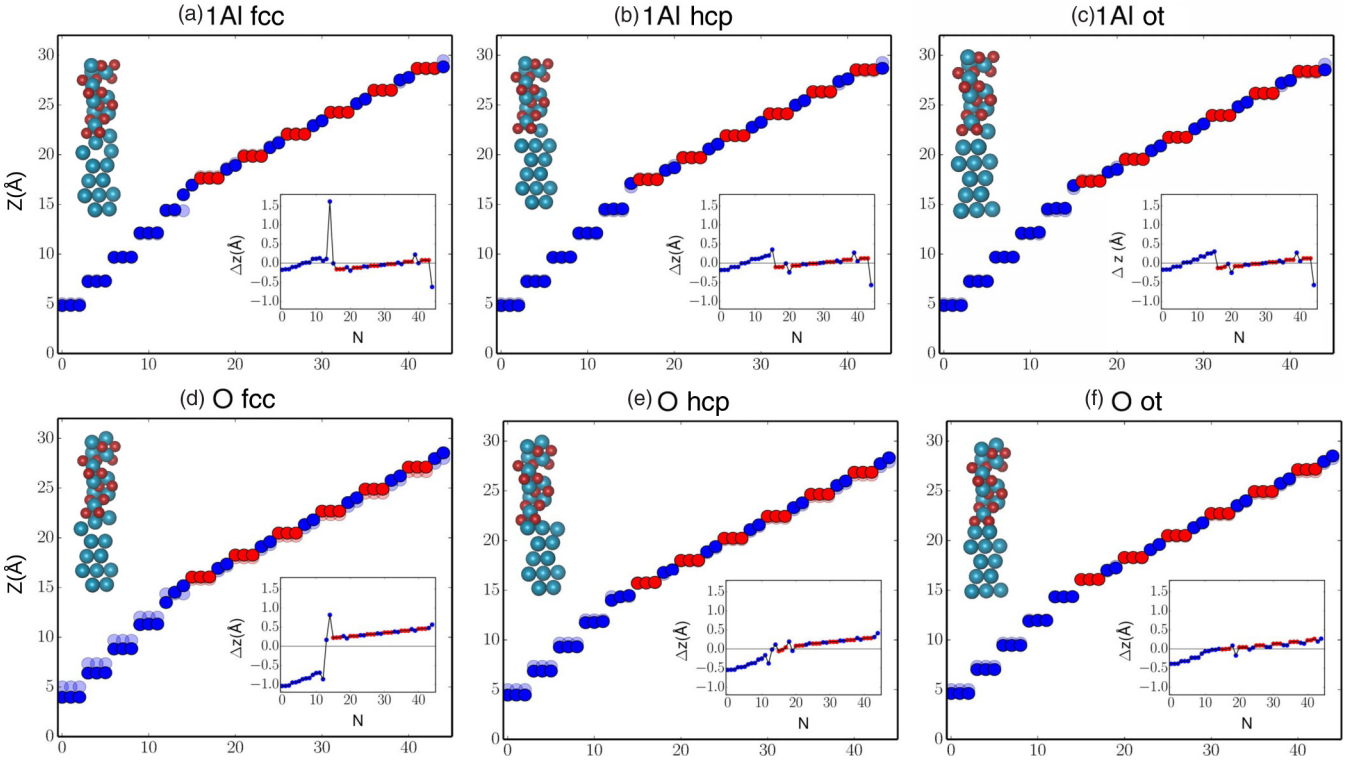

FIG. 4. Atomic relaxation at the six interfaces along the z coordinate. (a–c) The Al-terminated cases. (d–f) The O-terminated cases. The blue circles represent Al atoms and the red ones represent O atoms. The light blue and red circles show the unrelaxed positions of the Al and O atoms, respectively. The insets show the changes in the z coordinates for each atom with respect to its unrelaxed position. N is the index of the atom counted from the bottom of the junction, and increasing with the z coordinate. The images in the upper left corners of the panels are the relaxed geometries from the simulations.

tunnel barrier, and it not only widens the metal-oxide transition region but also lowers the barrier height. This can be explained by the fact that a disordered and scarce distribution of Al atoms near the interface causes a smeared and reduced charge density in this area compared to the bulk metal. The more scarce the Al atom distribution is, the smaller the charge density, and the higher the electrostatic potential at the interface. The affected electrostatic potential changes the relative positions of the Fermi level of the metal and the conduction-band edge of the oxide, which defines the height of the tunnel barrier. However, the positions of the energy levels depend not only on the spatial configuration of the atoms but also on the possible charge transfer at the interface. Explaining the band alignment needs a more detailed investigation of the charge densities and the potentials for different interface geometries. In this paper, we focus solely on the geometrical properties of the junctions.

E. Interlayer relaxations in Al/α-Al_2O_3 systems

Besides introducing irregularities at the surfaces of the metal films, relaxation effectively changes the thicknesses of the insulating layers in metal-oxide systems. This is due to acquirement of Al atoms from the metal surface and/or due to the changes in the interplanar distances in the oxide. The variation in the insulator thickness throughout a MIM junction is a commonly observed phenomenon in experiments. It highly affects the operation of MIM devices, since the tunneling probability depends exponentially on the barrier width. Even though the most probable reason for the thickness variations in experiments could be the varying number of layers, changes in thicknesses due to interplanar relaxations might further enhance the nonuniformity within a sample. This means that the thickness of an oxide composed of a defined number of layers might still vary along the junction because of the differences in the local geometries in different regions of the interface.

To find out how far the influence of the interfacial geometry extends in the junction, we examine the relaxations of the interlayer distances beyond the interfaces. Figure 5 shows the interlayer relaxations Δd relative to the bulk interlayer distances in the Al and Al_2O_3 parts of the studied systems along with the results for the respective isolated slabs. The numbers of layers correspond to those in the Al or Al_2O_3 films before the relaxation of the total system. Thus, additional layers appearing due to the interface relaxation are omitted in order to enable comparison to the pristine metal or oxide surfaces.

Interlayer relaxations of the oxides significantly depend on the geometry of the interface. The consequent interplanar distances and the numbers of the affected layers vary among the examined junctions. For the Al-terminated oxides, the influence of the interfacial structures on the interplanar relaxations extends up to the fourth interlayer (involving the first five layers), after which Δd do not differ notably regardless of the interface type [Fig. 5(a)]. The span of the affected four interlayers amounts to 2.9 Å for the fcc stacking, and 2.6 Å for the hcp and ot stackings. These values are smaller

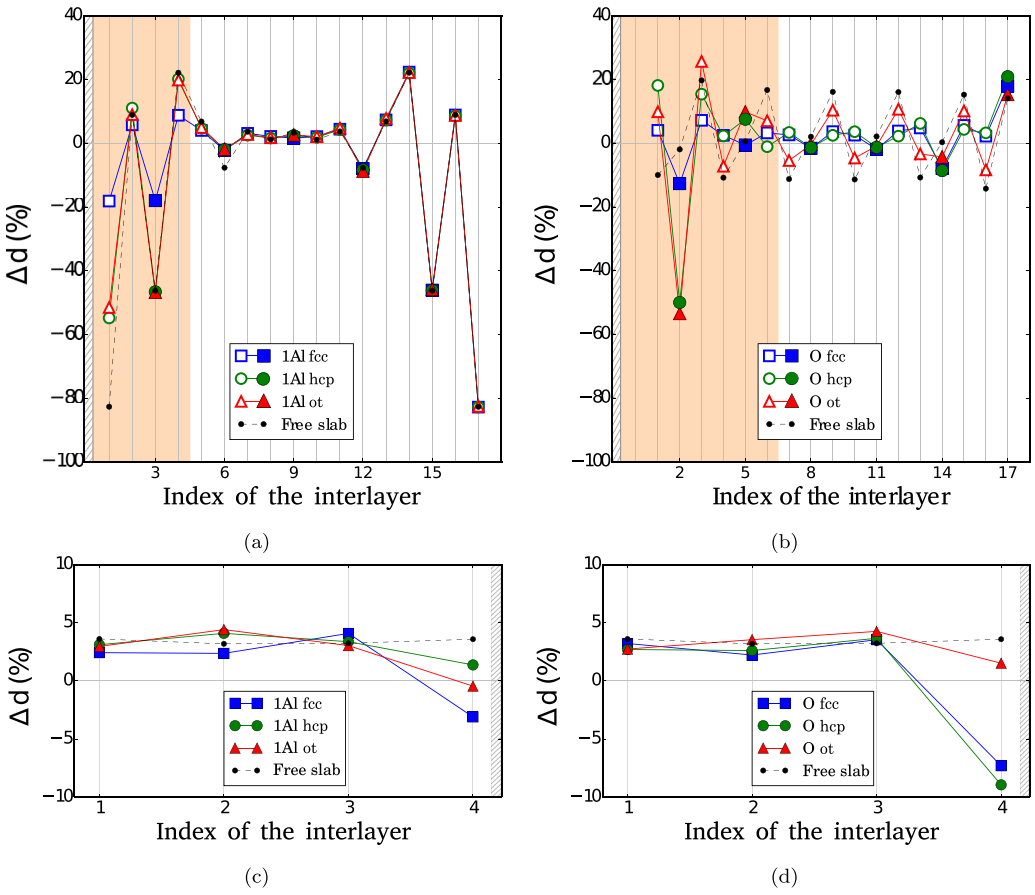

FIG. 5. Interplanar space relaxation Δd relative to the bulk interlayer distances in the metal and the oxide films of Al/Al_2O_3 junctions. (a, b) Al_2O_3 parts in the Al- and O-terminated junctions, respectively, (c, d) Al metal parts in the Al- and O-terminated junctions, respectively. Hatched regions at the edges of the plots show the positions of the interfaces. Filled and open data points correspond to the Al-Al and Al-O interplanar distances, respectively. Shaded regions in (a) and (b) mark the impact span of the interface geometry on interplanar relaxations. The number of layers falling in the shaded regions, $N = 5$ (four interlayers) for the Al-terminated structures, and $N = 7$ (six interlayers) for the O-terminated cases.

than the corresponding value in the bulk oxide (3 Å), and suggest the reduction in the total thickness of the oxide film due to interplanar relaxations. Thus, in all the Al-terminated oxides, the first four interlayers [marked with shaded regions in Fig. 5(a)] experience net contractions relative to the bulk geometry. The contractions amount to as much as 13% for 1Al hcp and 1Al ot, and to 3% for 1Al fcc. This indicates that in the Al-terminated structures up to the first five layers of Al_2O_3 are responsible for the thickness variation in the oxide films. The magnitude of the impact depends on the stacking sequence at the interface.

In the case of the O-terminated oxides, interplanar relaxations are dependent on the interface geometry up to the sixth interlayer (involving the first seven layers) in the O fcc and O hcp structures [Fig. 5(b)]. In the O ot junction, the relaxed interplanar distances qualitatively follow the other two cases only up to the third interlayer. Opposite to the Al-terminated junctions, the total thicknesses of the first six interlayers in the O-terminated oxides [marked with the shaded region in Fig. 5(b)] are expanded by 2% relative to the bulk case, and amount to 4.4 Å. Thus, in the O-terminated structures, up to seven layers might be responsible for affecting the thickness of the oxide. The magnitude of the impact is independent of the interface geometry, in contrast to the Al-terminated cases.

Our findings are summarized in Table V. An overall impact of the interplanar relaxations on the thicknesses of the oxides is either contraction or expansion depending on the interface geometry. The O-terminated oxides experience expansion,

TABLE V. Effect of interplanar relaxations on the barrier thicknesses in different Al/Al_2O_3 junctions. N is the number of the layers used in evaluating the thickness variation of the oxide (see text and Fig. 5). d_N is the net thickness of the N layers. Δd_N is the net change in the thickness of the barrier relative to the bulk structure. s is the width of the barrier from Ref. [6].

	N	d_N(Å)	Δd_N(%)	s(Å)
1Al fcc	5	2.9	−3	8.9
1Al hcp	5	2.6	−13	6.8
1Al ot	5	2.6	−13	7.6
O fcc	7	4.4	+2	10.3
O hcp	7	4.4	+2	10.5
O ot	7	4.4	+2	9.7

TABLE VI. Equilibrium lattice constants (a_0), bulk moduli (B), and cohesive energies (E_c) of bulk Al and Al_2O_3. The error percentages are given with respect to the experimental values listed in the last row.

	Al						Al_2O_3							
	a_0 (Å)	Error (%)	B (GPa)	Error (%)	E_c (eV/atom)	Error (%)	a_0 (Å)	Error (%)	c_0 (Å)	Error (%)	B (GPa)	Error (%)	E_c (eV/Al_2O_3)	Error (%)
LDA	3.99	−1.48	84.1	6.01	4.00	17.99	4.749	−0.21	12.967	−0.18	258.2	1.57	36.35	14.31
PBE	4.04	−0.25	77.9	−1.86	3.43	1.18	4.829	1.47	13.184	1.49	230.2	−9.44	30.59	−3.81
PW91	4.05	0.0	74.4	−6.27	3.38	−0.29	4.821	1.30	13.164	1.33	234.0	−7.95	31.27	−1.67
Experiment	4.05 [34]		79.38 [50]		3.39 [51]		4.759 [35]		12.991 [35]		254.2 [52]		31.8 [53]	

while the Al-terminated oxides contract. The impact is less dramatic in the O-terminated cases. Among the Al-terminated structures, the thicknesses of the oxides are affected significantly more strongly in the 1Al hcp and 1Al ot geometries compared to 1Al fcc. The obtained results are in a gratifying agreement with our previous estimates for the barrier widths s based on the experimental current-voltage characteristics for the $Al/Al_2O_3/Al$ junction. Table V shows that the largest barrier widths correspond to the O-terminated junctions, next follows 1Al fcc, and, finally, the smallest barrier widths correspond to 1Al hcp and 1Al ot, consistent with the current results.

Interplanar relaxations in the metal parts are illustrated in Figs. 5(c) and 5(d) for the Al- and O-terminated junctions, respectively. In all the geometries, the first three interplanar spacings experience slight expansions (<5%), similar to the pristine slab. This is due to the lateral compressive strain on the Al metal film needed to match the lattice constant of the oxide. The effect was verified for Au(001) in Au(001)/Fe(001) junctions in Ref. [49]. It was also shown that the change in the interlayer distances closer to the interface (index 4 in our case) is not an artefact of the compressive strain on the metal, which is also visible in our results, since the Δd values for the named interlayers differ in magnitude as well as in sign for different junctions. Nevertheless, these interplanar relaxations are significantly smaller than those observed in the oxide parts, even though the Al parts experience stronger atomic displacements at the interface compared to the oxide parts as described in the previous section.

IV. SUMMARY

We have studied in detail the structures of six Al/Al_2O_3 interfaces and their roles in formation of the tunnel barrier profiles using first-principles DFT modeling. We have checked the accuracy of the methods commonly used in existing works on Al/Al_2O_3 interfaces. These are the exchange-correlation functionals, the universal binding-energy relation, and the ideal work of separation. We have found that PBE is the most relevant functional for describing Al/Al_2O_3 systems, and that the higher-order spline interpolation outperforms the UBER fit for finding equilibrium interfacial distances and adhesion energies. In addition, we have challenged the interpretation of the ideal work of separation as a measure of the junction stability and have shown that it might be misleading in predicting the optimal structures. Instead, total binding energies of the studied junction models could be more relevant for estimating the overall stability of the systems.

After carefully obtaining the stable structures, we have thoroughly characterized the atomic and interplanar relaxations in the junctions. The oxide films undergo strong, interface-dependent interplanar relaxations near the interfaces, which span up to the fifth layer for the Al-terminated structures and up to the seventh layer for the O-terminated structures. Beyond these layers, interplanar relaxations are independent of the interface geometry. The initially Al-terminated oxides tend to decrease their thickness, while the O-terminated ones experience expansion.

By examining the systems with identical numbers of layers, we have identified the three main contributions having a significant effect on the electron tunnel barrier parameters: (i) interplanar relaxations in the oxide beyond the immediate interface, which contribute to the variation of the barrier width; (ii) irregularities on the metal film surface, which lower the barrier height and expand the metal-oxide transition region; and (iii) extension of the oxide layers by adopting Al atoms from the metal surface, which expands the total width of the barrier. The gained information provides an insight into the correlation between the detailed atomic structure and the tunnel barrier parameters determining the performance of MIM devices.

TABLE VII. Changes in the interplanar spacings Δd of the Al(111) and Al-terminated Al_2O_3 (0001) slabs following the relaxations, predicted with the different exchange-correlation functionals. The Δd values are given in percentages relative to the unrelaxed structures.

	Interlayer		LDA	PBE	PW91	Experiment	
Al	1-2		−1.1	+1.1	+1.3	+1.7 [56]	+0.9 [57]
	2-3		−2.4	0.0	+0.3	+0.5 [56]	
Al_2O_3	1-2	(Al − O_3)	−85.7	−82.6	−82.0	–51 [54]	–50 [55]
	2-3	(O_3-Al)	+3.3	+8.8	+8.6	+16 [54]	+6 [55]
	3-4	(Al − O_3)	−44.2	−46.2	−46.2	–29 [54]	
	4-5	(O_3-Al)	+19.2	+22.2	+22.1	+20 [54]	

TABLE VIII. Surface energies in joules per square meter for Al(111) and Al-terminated Al_2O_3 (0001) slabs calculated with the LDA, PBE, and PW91 exchange-correlation functionals. The values without references represent our results.

	Al			Al_2O_3		
LDA	0.98,	1.02 [14],	0.88 [58]	2.01,	2.12 [14],	1.98 [59]
PBE	0.84,	0.77 [58],	0.81 [17]	1.64,	1.54 [17]	
PW91	0.79,	0.81 [14]		1.66,	1.54 [60],	1.59 [14]
Experiment	1.14 [61]			1.69 [62],	2.6 [63]	

ACKNOWLEDGMENTS

We acknowledge the computational resources provided by the Aalto Science-IT project. This work was supported by the Academy of Finland through its Centres of Excellence Programme (2012–2017) under Project No. 251748.

APPENDIX: COMPARISON OF LDA, PBE, AND PW91 EXCHANGE-CORRELATION FUNCTIONALS

1. Bulk Al and α-Al_2O_3

Table VI shows the bulk parameters for Al and Al_2O_3, calculated with the PBE, PW91, and LDA exchange-correlation functionals. Errors with respect to the known experimental data are also provided. Since experimental measurements are performed at finite temperatures, values extrapolated to 0 K are used where available.

Among the considered functionals, PW91 gives the most accurate results for the lattice constant and the cohesive energy of Al with respect to the experimental values, while PBE predicts its bulk modulus most accurately. LDA gives the most precise lattice constants and bulk modulus for Al_2O_3; however, it notably overestimates the cohesive energies of both Al and Al_2O_3.

2. Al(111) and Al_2O_3(0001) surfaces

Table VII presents comparison of the three exchange-correlation functionals in predicting the surface relaxations of Al and Al_2O_3. For the Al surface, both PBE and PW91 predict slight expansion of the first two interlayers in agreement with experiments, while LDA suggests contraction of the same interlayers. The tendency of LDA to predict the contraction of the first two interlayers in Al has also been observed for other metals when experimental lattice constants are used [58]. The surface relaxation of Al_2O_3 is described equally reasonably by all three functionals, considering that the experimental data for the changes in interlayer separations of Al_2O_3 exhibit a large scatter, not only with respect to the magnitudes but also with respect to the sign [22,54,55].

Surface energies of Al and Al_2O_3 slabs are given in Table VIII. Our calculated surface energies are in good agreement with other theoretical works. However, to our knowledge, there is a lack of experimental data for the Al(111) and Al_2O_3 (0001) surface energies. In addition, they differ notably for Al_2O_3. This makes it difficult to evaluate the accuracy of the exchange-correlation functionals in predicting surface energies. Taking an average experimental value for Al_2O_3 as a reference, LDA produces more accurate values than PBE and PW91. Among the two GGAs, the total error produced by PBE is smaller than that of PW91.

[1] P. Seidel, *Applied Superconductivity: Handbook on Devices and Applications*, Encyclopedia of Applied Physics Vol. 1 (Wiley, New York, 2015).

[2] A. Narlikar, *The Oxford Handbook of Small Superconductors*, Oxford Handbooks (Oxford University Press, New York, 2017).

[3] H. Jung, Y. Kim, K. Jung, H. Im, Y. A. Pashkin, O. Astafiev, Y. Nakamura, H. Lee, Y. Miyamoto, and J. S. Tsai, Phys. Rev. B **80**, 125413 (2009).

[4] N. Alimardani, E. W. Cowell III, J. F. Wager, J. F. Conley, Jr., D. R. Evans, M. Chin, S. J. Kilpatrick, and M. Dubey, J. Vac. Sci. Technol. A **30**, 01A113 (2012).

[5] L. Zeng, D. T. Tran, C.-W. Tai, G. Svensson, and E. Olsson, Sci. Rep. **6**, 29679 (2016).

[6] M. Koberidze, A. V. Feshchenko, M. J. Puska, R. M. Nieminen, and J. P. Pekola, J. Phys. D **49**, 165303 (2016).

[7] V. F. Maisi, O.-P. Saira, Y. A. Pashkin, J. S. Tsai, D. V. Averin, and J. P. Pekola, Phys. Rev. Lett. **106**, 217003 (2011).

[8] T. Greibe, M. P. V. Stenberg, C. M. Wilson, T. Bauch, V. S. Shumeiko, and P. Delsing, Phys. Rev. Lett. **106**, 097001 (2011).

[9] L. Zeng, S. M. Nik, T. Greibe, P. Krantz, C. Wilson, P. Delsing, and E. Olsson, J. Phys. D **48**, 395308 (2015).

[10] H. Kohlstedt, F. König, P. Henne, N. Thyssen, and P. Caputo, J. Appl. Phys. **80**, 5512 (1996).

[11] J. F. Conley and N. Alimardani, in *Rectenna Solar Cells*, edited by G. Moddel and S. Grover (Springer, New York, 2013), pp. 111–134.

[12] W. Zhang and J. R. Smith, Phys. Rev. Lett. **85**, 3225 (2000).

[13] I. G. Batyrev and L. Kleinman, Phys. Rev. B **64**, 033410 (2001).

[14] D. J. Siegel, L. G. Hector, and J. B. Adams, Phys. Rev. B **65**, 085415 (2002).

[15] M. Dieška, M. Konôpka, and P. Bokes, Surf. Sci. **601**, 4134 (2007).

[16] E.-G. Kim and J.-L. Brédas, Org. Electron. **14**, 569 (2013).

[17] Y. Liu and X.-S. Ning, Comput. Mater. Sci. **85**, 193 (2014).

[18] G. Pilania, B. J. Thijsse, R. G. Hoagland, I. Lazić, S. M. Valone, and X.-Y. Liu, Sci. Rep. **4**, 4485 (2014).

[19] T. DuBois, M. Cyster, G. Opletal, S. Russo, and J. Cole, Mol. Simul. **42**, 542 (2016).

[20] R. S. Timsit, W. G. Waddington, C. J. Humphreys, and J. L. Hutchison, Appl. Phys. Lett. **46**, 830 (1985).

[21] D. Medlin, K. McCarty, R. Hwang, S. Guthrie, and M. Baskes, Thin Solid Films **299**, 110 (1997).

[22] J. Toofan and P. Watson, Surf. Sci. **401**, 162 (1998).

[23] G. Dehm, B. Inkson, and T. Wagner, Acta Mater. **50**, 5021 (2002).
[24] D. Flötotto, Z. Wang, and E. Mittemeijer, Surf. Sci. **633**, 1 (2015).
[25] L. Jeurgens, W. Sloof, F. Tichelaar, and E. Mittemeijer, Surf. Sci. **506**, 313 (2002).
[26] A. Bianconi, R. Z. Bachrach, S. B. M. Hagstrom, and S. A. Flodström, Phys. Rev. B **19**, 2837 (1979).
[27] N. Watari, M. Saito, H. Tsuge, O. Sugino, and S. Ohnishi, Jpn. J. Appl. Phys. **39**, L479 (2000).
[28] A. Kiejna and B. Lundqvist, Surf. Sci. **504**, 1 (2002).
[29] J. J. Mortensen, L. B. Hansen, and K. W. Jacobsen, Phys. Rev. B **71**, 035109 (2005).
[30] J. Enkovaara, C. Rostgaard, J. J. Mortensen, J. Chen, M. Dułak, L. Ferrighi, J. Gavnholt, C. Glinsvad, V. Haikola, H. A. Hansen, H. H. Kristoffersen, M. Kuisma, A. H. Larsen, L. Lehtovaara, M. Ljungberg, O. Lopez-Acevedo, P. G. Moses, J. Ojanen, T. Olsen, V. Petzold, N. A. Romero, J. Stausholm-Møller, M. Strange, G. A. Tritsaris, M. Vanin, M. Walter, B. Hammer, H. Häkkinen, G. K. H. Madsen, R. M. Nieminen, J. K. Nørskov, M. Puska, T. T. Rantala, J. Schiøtz, K. S. Thygesen, and K. W. Jacobsen, J. Phys.: Condens. Matter **22**, 253202 (2010).
[31] J. P. Perdew and Y. Wang, Phys. Rev. B **45**, 13244 (1992).
[32] J. P. Perdew, K. Burke, and M. Ernzerhof, Phys. Rev. Lett. **77**, 3865 (1996).
[33] J. P. Perdew, J. A. Chevary, S. H. Vosko, K. A. Jackson, M. R. Pederson, D. J. Singh, and C. Fiolhais, Phys. Rev. B **46**, 6671 (1992).
[34] R. Wyckoff, *Crystal Structures*, Crystal Structures Vol. 1 (Wiley, New York, 1963).
[35] R. E. Newnham and Y. M. de Haan, Z. Kristallogr. **117**, 235 (1962).
[36] F. Murnaghan, Proc. Natl. Acad. Sci. USA **30**, 244 (1944).
[37] S. Oktyabrsky and P. Ye, *Fundamentals of III-V Semiconductor MOSFETs* (Springer, New York, 2010).
[38] M. W. Finnis, J. Phys.: Condens. Matter **8**, 5811 (1996).
[39] *IUPAC. Compendium of Chemical Terminology*, 2nd ed., edited by A. D. McNaught and A. Wilkinson (Blackwell, Oxford, 1997), XML on-line corrected version at http://goldbook.iupac.org (2006) created by M. Nic, J. Jirat, and B. Kosata with updates compiled by A. Jenkins.
[40] A. Banerjea and J. R. Smith, Phys. Rev. B **37**, 6632 (1988).
[41] J. H. Rose, J. Ferrante, and J. R. Smith, Phys. Rev. Lett. **47**, 675 (1981).
[42] J. H. Rose, J. R. Smith, and J. Ferrante, Phys. Rev. B **28**, 1835 (1983).
[43] J. G. Simmons, J. Appl. Phys. **34**, 1793 (1963).
[44] N. Arakawa, Y. Otaka, and K. Shiiki, Thin Solid Films **505**, 67 (2006).
[45] J. Jung, Y. Kim, and H. Im, J. Korean Phys. Soc. **55**, 2512 (2009).
[46] K. Mistry, M. Yavuz, and K. P. Musselman, J. Appl. Phys. **121**, 184504 (2017).
[47] M. Z. Diešková, A. Ferretti, and P. Bokes, Phys. Rev. B **87**, 195107 (2013).
[48] D. Shen, R. Zhu, W. Xu, J. Chang, Z. Ji, G. Sun, C. Cao, and J. Chen, Chin. Sci. Bull. **57**, 409 (2012).
[49] M. Benoit, C. Langlois, N. Combe, H. Tang, and M.-J. Casanove, Phys. Rev. B **86**, 075460 (2012).
[50] G. N. Kamm and G. A. Alers, J. Appl. Phys. **35**, 327 (1964).
[51] C. Kittel, in *Introduction to Solid State Physics*, 7th ed. (Wiley, New York, 2007), p. 57.
[52] J. H. Gieske and G. R. Barsch, Phys. Status Solidi B **29**, 121 (1968).
[53] W. Haynes, *CRC Handbook of Chemistry and Physics*, 94th ed. (Taylor & Francis, London, 2013).
[54] P. Guénard, G. Renaud, A. Barbier, and M. Gautier-Soyer, Surf. Rev. Lett. **05**, 321 (1998).
[55] E. A. Soares, M. A. Van Hove, C. F. Walters, and K. F. McCarty, Phys. Rev. B **65**, 195405 (2002).
[56] J. R. Noonan and H. L. Davis, J. Vac. Sci. Technol. A **8**, 2671 (1990).
[57] H. B. Nielsen and D. L. Adams, J. Phys. C **15**, 615 (1982).
[58] J. L. D. Silva, C. Stampfl, and M. Scheffler, Surf. Sci. **600**, 703 (2006).
[59] R. Di Felice and J. E. Northrup, Phys. Rev. B **60**, R16287(R) (1999).
[60] H. P. Pinto, R. M. Nieminen, and S. D. Elliott, Phys. Rev. B **70**, 125402 (2004).
[61] W. Tyson and W. Miller, Surf. Sci. **62**, 267 (1977).
[62] J. M. McHale, A. Navrotsky, and A. J. Perrotta, J. Phys. Chem. B **101**, 603 (1997).
[63] N. Alexandra, Geochem. Trans. **4**, 34 (2003).